1.3 Energy Scale and Spectral Redistribution Function

1.3.1 Energy Scale and Spectral Resolution

1.3.1.1 Purpose

The purpose of this section is to present the correct response from incident X-ray energy to detected pulse height for the ACIS flight instrument. Also presented is the spectral resolution of the ACIS flight devices.

1.3.1.2 Measurements

The XRCF energy scale and spectral resolution results presented here have been based on phase I telemetry data.

XRCF phase I was performed with the ACIS flight instrument, but without the High Resolution Mirror Assembly or the gratings. The full ACIS focal plane was illuminated with X-rays from either the Electron-Impact Point Source or the Double Crystal Monochrometer.

During XRCF phase I, the detector electronics temperature was 13° C and the focal plane temperature was $-110°$ C.

ACIS was run in the full frame timed exposure mode, with a 3.34 second exposure time. During most science runs, six of the CCDs were read out simultaneously. A single science run included a number of TRW IDs, and in a few cases multiple energies as well. Subarrays of various sizes were used to avoid telemetry saturation.

Table 1.4 describes each of the science runs used in this section.

1.3.1.3 Data Processing

The ACIS FEP processing mode was timed exposure faint 3x3 with an event threshold of 38 ADU for the front illuminated devices and 20 ADU for the back illuminated devices. The split threshold was 13 ADU for all measurements.

Science Run	Source	Energy eV	FI Window Rows	BI Window Rows	CCDs	TRW IDs
69	EIPS O-K	525	500	156	s0 s2 s4-5	
70	EIPS O-K	525	250	78	s0-5	I-IAS-EA-2.001 - 2.006
71	EIPS O-K	525	250	78	i0-3 s2-3	I-IAI-EA-1.001 - 1.004
72	EIPS Si-K	1740	56	50	s0 s2 s4-5	I-IAS-EA-2.013 - 2.018
75	EIPS Si-K	1740	56	50	i0-3 s2	I-IAI-EA-1.009 - 1.012
77	EIPS Fe-K	6399	46	46	i0-3 s3	
78	EIPS Fe-K	6399	46	46	i0-1 i3 s3	I-IAI-EA-1.025 - 1.028
83	EIPS Fe-K	6399	46	46	i0-2 s2-3	I-IAI-EA-1.028
84	EIPS Fe-K	6399	46	46	s0-5	I-IAS-EA-2.037 - 2.042
91	EIPS Cu-K	8040	30	30	i0-3 s2-3	I-BND-BU-2.004
92	EIPS Cu-K	8040	20	30	i0-3 s2-3	I-IAI-EA-1.029 - 1.032
93	EIPS Cu-K	8040	20	30	s0-5	I-IAS-EA-2.043 - 2.048
96	EIPS C-K	277	1024	512	s0-5	I-BND-BU-2.037
97	EIPS C-K	277	512	1024	s0-5	I-IAS-EA-2.049 - 2.050
100	EIPS Ti-K	4509	28	24	s0-5	I-IAS-EA-2.032, 2.034
104	EIPS Ti-K	4509	28	24	i0-3 s2-3	I-IAI-EA-1.024
111	EIPS Al-K	1487	24	20	s0-5	I-IAS-EA-2.029 - 2.031
112	EIPS Al-K	1487	24	20	i0-3 s2-3	I-IAI-EA-1.017 - 1.020
114	EIPS Si-K	1740	28	26	i0-3 s2	I-IAI-EA-5.003 - 5.004
115	EIPS O-K	525	250	78	i0-3 s2-3	I-IAI-EA-5.001 - 5.002
116	EIPS O-K	525	250	78	s0-5	I-IAS-EA-2.101 - 2.106
117	EIPS O-K	525	250	78	i0-3 s2-3	I-IAI-EA-1.101 - 1.104
120	EIPS Ti-K	4509	28	24	s0-5	I-IAS-EA-2.131 - 2.132, 2.134
122	EIPS Ti-K	4509	28	24	s0-5	I-IAS-EA-2.133, 2.135 - 2.136
123	EIPS Ti-K	4509	28	24	i0-3 s2-3	I-IAI-EA-1.121 - 1.124
128	DCM	1380	1024	1024	i3 s1 s3	I-IAI-EA-1.204 - 1.206
131	DCM	1770	512	512	i3 s1 s3	I-IAI-EA-1.213 - 1.215
132	DCM	4500	1024	1024	i3 s1 s3	I-IAI-EA-1.222 - 1.224
149	DCM	2035	1024	1024	i0-3 s2-3	I-IAI-EA-1.225

Table 1.4: XRCF Phase I ACIS Science Run Descriptions

The ACIS BEP processing mode was timed exposure Faint mode with a window filter. The size of the windows varied depending on the flux rate, from as tiny as 20 rows to as many as the full 1024. In all cases, the windowing was split into two strips, one toward the top of the CCD and one toward the bottom of the CCD. Because of the differences in the quantum efficiency of the front illuminated devices from the back illuminated devices, different window sizes were used for the front illuminated and back illuminated devices. The window sizes used in each data set are listed in Table 1.4.

The flight software telemetry packets were converted to FITS format average bias files and ERV format event lists using PSCI (for a description of the formats and the PSCI program see http://acis.mit.edu/ttools/psci.html).

The average bias and the ERV format event lists were combined and converted to ARV format event lists using an IDL script. The IDL script subtracted the delta overclock value and the average bias values for each pixel of each event.

Each ARV format event list was then summarized using an IDL script. This IDL script fit a gaussian to the main peak of the spectrum. Only events in ACIS grade bit map 0x1d05 0x0047 0x0004 0x0047 0x1133 0x0003 0x1100 0x0000 0x1d04 0x0000 0x0004 0x0000 0x0000 0x0003 0x0000 0x0000 (ASCA grades 02346) were considered. Using the fit parameters, the position of the peak, full width half max of the peak (defined to be 2.35 times the fitted sigma), and total number of counts under the peak are determined. The number of counts under the peak is taken to be $\sqrt{2\pi}\sigma N_{max}$, where N_{max} is the number of counts in the peak channel. The IDL script computes the flux in counts per centimeter squared per second assuming a frame time of 3.34 seconds and an input window size. All of these values are written to a text format file.

Finally, the text format summary files are read by another IDL script which uses the peak location and peak width values at each energy to tabulate and plot the linear energy scale and spectral resolution values. This script also applies a pileup correction and the filter efficiency to the counts under the peak. See Section 1.4 for a description of pileup.

1.3.1.4 Results

The slope, intercept, and RMS deviation of a linear fit of the energy scale of the ACIS flight devices are listed in Table 1.5. Pulse height as a function of energy is fit to the relation $PH(ADU) = Slope \times Energy(eV) + Intercept$.

CCD	Quadrant A			Quadrant B			Quadrant C			Quadrant D		
	Slope ADU/eV	Intercept ADU	RMS eV	Slope ADU/eV	Intercept ADU	RMS eV	Slope ADU/ev	Intercept ADU	RMS eV	Slope ADU/eV	Intercept ADU	RMS eV
i0	0.2636	0.81	3.75	0.2573	0.65	4.03	0.2662	0.77	3.52	0.2582	0.60	4.06
i1	0.2622	0.38	3.50	0.2559	-0.09	3.97	0.2596	0.36	4.34	0.2616	0.07	3.80
i2	0.2731	-0.98	3.10	0.2839	-1.07	3.35	0.2825	0.07	3.59	0.2745	0.43	3.67
i3	0.2582	1.19	4.68	0.2588	1.25	4.65	0.2542	1.25	4.51	0.2592	1.09	4.55
s0	0.2725	-0.12	4.69	0.2677	-0.54	3.35	0.2574	0.13	4.02	0.2565	-0.34	3.40
s1	0.2359	-22.00	14.80	0.2182	-27.07	22.37	0.2234	-24.86	20.23	0.2297	-25.33	18.84
s2	0.2602	0.03	3.75	0.2715	0.15	5.27	0.2640	-0.51	4.25	0.2692	-0.54	6.33
s3	0.2262	-17.33	11.16	0.2158	-19.88	13.99	0.2186	-19.65	13.18	0.2273	-22.80	13.66
s4	0.2328	-1.09	3.80	0.2272	-0.58	6.16	0.2301	-0.72	5.76	0.2391	-0.96	4.55
s5	0.2534	-0.16	3.09	0.2576	-0.13	3.18	0.2601	0.18	2.70	0.2114	0.46	4.32

Table 1.5: Energy Scale for ACIS Flight Devices

The residual errors from the linear energy scale fit for the front illuminated devices are shown in Figure 1.5. The residual errors from the linear energy scale fit for the back illuminated devices are shown in Figure 1.6. Note that Figure 1.5 and Figure 1.6 are on different vertical scales. Random errors for the line center locations are much less than 1 eV.

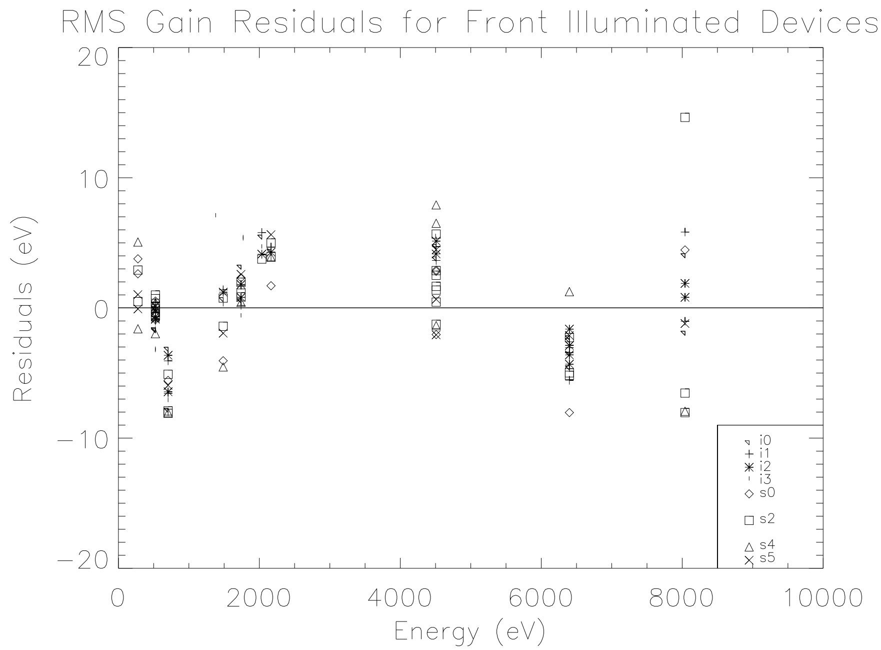

Figure 1.5: Linear Energy Scale Residuals for the Front Illuminated Devices

The FWHM for the ACIS flight devices is shown in Figure 1.7. In Figure 1.7 the points for the front illuminated devices are the average of the four quadrants, while the points for the back illuminated devices show each quadrant separately. The values for the front illuminated devices are listed in Table 1.6. The values for the back illuminated devices are listed in Table 1.7. The "NA" indicates that a data point is not available. The 277 eV measurement was made only for the S-array. Many of the DCM energies were taken with only i3, s1 and s3 on. One of the DCM sets was taken with only the I-array.

The spectral resolution as a function of energy for the front illuminated devices is shown as a solid line in Figure 1.7 and is described by

$$FWHM(E) = \sqrt{(FWHM_0)^2 + 2.35^2 Fano \times w \times E} \tag{1.4}$$

Note that here we treat $FWHM_0$ as an empirical parameter. In the simplest model for spectral resolution (see section 1.1) one expects

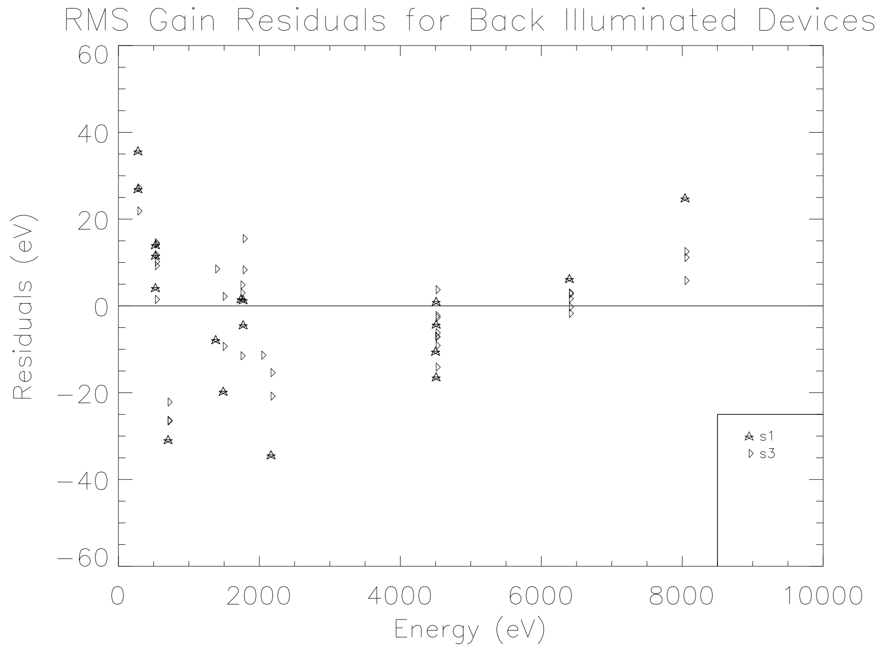

Figure 1.6: Linear Energy Scale Residuals for the Back Illuminated Devices

Energy	277	525	1380	1487	1740	1770	2035	4500	4509	6399	8040
Source	C-K	O-K	DCM	Al-K	Si-K	DCM	DCM	DCM	Ti-K	Fe-K	Cu-K
i0	NA	50.8	NA	73.7	83.7	NA	81.8	NA	120.4	145.9	169.5
i1	NA	50.9	NA	73.3	83.1	NA	80.7	NA	119.9	145.1	169.7
i2	NA	53.7	NA	77.8	89.4	NA	85.6	NA	128.7	155.2	179.1
i3	NA	49.6	67.0	71.8	81.8	77.4	79.7	114.5	118.6	144.0	168.2
s0	45.8	54.9	NA	77.3	86.7	NA	NA	NA	123.5	149.8	175.7
s2	39.6	52.0	NA	74.6	84.6	NA	82.7	NA	122.6	149.0	172.2
s4	37.3	49.8	NA	69.5	78.9	NA	NA	NA	111.3	134.9	159.9
s5	38.8	48.4	NA	69.2	79.3	NA	NA	NA	113.3	137.3	161.4

Table 1.6: Average FWHM (eV) for Front Illuminated Devices

$$FWHM_0 = 2.35 \times \sigma \times w \tag{1.5}$$

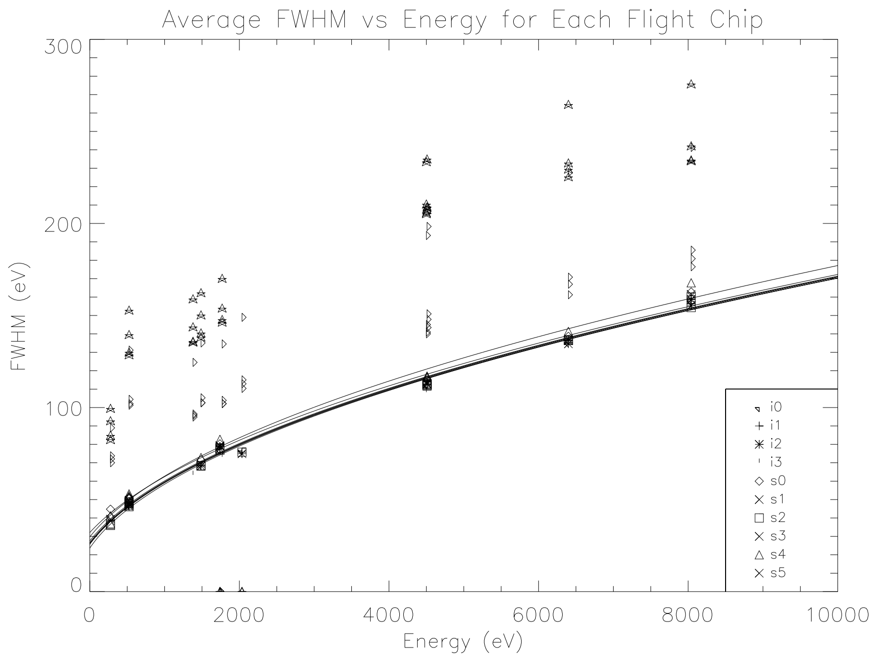

Figure 1.7: Average FWHM versus Energy

	Energy	277	525	1380	1487	1740	2035	4500	4509	6399	8040
	Source	C-K	O-K	DCM	Al-K	DCM	DCM	DCM	Ti-K	Fe-K	Cu-K
s1	A	92.8	139.6	143.8	150.3	154.0	NA	205.9	209.0	232.8	242.1
	B	82.6	128.6	135.9	140.5	147.8	NA	205.3	208.6	225.3	234.5
	C	84.9	130.1	135.5	138.2	146.4	NA	210.5	207.5	229.5	234.0
	D	99.5	152.9	159.0	162.3	170.1	NA	233.5	235.0	264.6	275.8
s3	A	73.7	104.5	96.5	105.3	103.9	115.0	141.0	147.4	167.0	180.9
	B	72.1	101.3	95.8	102.6	102.2	110.4	145.1	150.8	170.8	185.5
	C	70.0	102.1	94.9	102.5	102.1	112.9	140.0	143.6	161.3	176.5
	D	89.0	131.2	124.5	135.1	134.5	149.0	193.5	199.4	227.7	241.3

Table 1.7: FWHM (eV) for Back Illuminated Devices

The expected value of $Fano \times w$ in silicon detectors at -120 ° C is $0.135 \times 3.73 = 0.504$
.

$FWHM_0$ and $Fano \times w$ for each quadrant of each front illuminated device is shown in Table 1.8.

Chip	$FWHM_0$	$Fano \times w$
i0	26.56	0.516
i1	26.49	0.517
i2	26.02	0.513
i3	23.77	0.514
s0	32.09	0.519
s2	25.88	0.509
s4	29.73	0.552
s5	27.56	0.518

Table 1.8: Average Front Illuminated Devices $FWHM_0$ and $Fano \times w$

1.3.1.5 CSR Energy Scale Linearity and Spectral Response Valid Data Summary

In addition to the data taken at XRCF, spectral resolution data was collected at CSR. These sets were taken with laboratory electroics identical in design to the flight DEA, but with gains different from the flight electronics. These data should be useful for future analyses of energy scale linearity and spectral response function shape. The data sets are listed in Tables 1.9 through 1.18.

The column labeled "Directory" is the location of the dataset from /ohno/di/database on the local CSR network.

In the column labeled "Rejected Frames" the letter "b" following the number indicates that the majority of the rejected frames were rejected due to pixels above the event threshold in the overclock region. The letter "n" following the number indicates that the majority of the rejected frames were rejected due to standard deviation of the overclocks exceeding the noise threshold.

The column labeled "Counts per Frame" contains the total number of G02346 events under the main peak for the data set.

Each data set included has been checked for by visual inspection of the data products and for consistency with other data sets.

The data products in each directory are summarized in Table 1.19. See MIT ACIS memo PS-71 dated 4 May 1995, by J. Woo (which can be found at http://acis.mit.edu/ttools/acis-analysis.html) for a detailed description of the file formats.

Chip	Target/Energy	Directory eV	Accepted Frames	Rejected Frames	Frame Time (seconds)	Counts per Frame
w203c4r/I0	al/1487	w203c4r/beavis/al/03jan97/2213	547	2b	3.277	4564.4
w203c4r/I0	cl/2622	w203c4r/beavis/cl/05jan97/0895	546	4b	3.277	2383.6
w203c4r/I0	v/4949	w203c4r/beavis/v/05jan97/0931	495	5b	3.277	4746
w203c4r/I0	v/4949	w203c4r/beavis/v/05jan97/1150	49	0n	3.276	4745.6
w203c4r/I0	fe/6399	w203c4r/beavis/fe/03jan97/2249	570	5b	3.277	4139.6
w203c4r/I0	co/6925	w203c4r/beavis/co/05jan97/1017	626	4b	3.277	3815.6
w203c4r/I0	ni/7471	w203c4r/beavis/ni/05jan97/1210	645	4b	3.277	3333.6
w203c4r/I0	ni/7471	w203c4r/beavis/ni/05jan97/1255	100	0n	3.277	3338
w203c4r/I0	zn/8630	w203c4r/beavis/zn/05jan97/1312	642	2b	3.277	2648.4
w203c4r/I0	zn/8630	w203c4r/beavis/zn/05jan97/1359	245	0n	3.277	2679.6
w203c4r/I0	ge/9875	w203c4r/beavis/ge/30dec96/2200	596	2b	3.277	2020.8
w203c4r/I0	ge/9875	w203c4r/beavis/ge/30dec96/2250	596	2b	3.277	2011.2

Table 1.9: w203c4r/I0 CSR Spectral Resolution Data Sets

Chip	Target/Energy	Directory eV	Accepted Frames	Rejected Frames	Frame Time (seconds)	Counts per Frame
w193c2/I1	al/1487	w193c2/butthead/al/22nov96/1819	646	2b	3.277	4577.2
w193c2/I1	p/2015	w193c2/butthead/p/27nov96/2228	174	1b	3.277	1705.2
w193c2/I1	cl/2622	w193c2/butthead/cl/25nov96/1921	648	1n	3.277	2425.6
w193c2/I1	cl/2622	w193c2/butthead/cl/25nov96/2002	324	0n	3.277	2422.8
w193c2/I1	v/4949	w193c2/butthead/v/22nov96/2001	644	6b	3.277	4806.4
w193c2/I1	fe55/5894	w193c2/butthead/fe55/30nov96/1214	594	1b	3.297	3360.8
w193c2/I1	fe/6399	w193c2/butthead/fe/22nov96/1913	644	1b	3.277	4170
w193c2/I1	co/6925	w193c2/butthead/co/29nov96/2002	644	2n	3.277	3840
w193c2/I1	co/6925	w193c2/butthead/co/29nov96/2041	97	2n	3.277	3836
w193c2/I1	ni/7471	w193c2/butthead/ni/29nov96/2300	150	0n	3.277	3426.8
w193c2/I1	ni/7471	w193c2/butthead/ni/29nov96/2323	643	3b	3.279	3404.8
w193c2/I1	zn/8630	w193c2/butthead/zn/22nov96/2050	633	6b	3.278	2501.6
w193c2/I1	zn/8630	w193c2/butthead/zn/22nov96/2141	490	2b	3.279	2496.8
w193c2/I1	ge/9875	w193c2/butthead/ge/25nov96/2027	635	5b	3.278	1982.4
w193c2/I1	ge/9875	w193c2/butthead/ge/25nov96/2108	650	NA	3.277	1983.6
w193c2/I1	ge/9875	w193c2/butthead/ge/25nov96/2148	191	1n	3.276	1998.8

Table 1.10: w193c2/I1 CSR Spectral Resolution Data Sets

Chip	Target/Energy	Directory eV	Accepted Frames	Rejected Frames	Frame Time (seconds)	Counts per Frame
w158c4r/I2	al/1487	w158c4r/butthead/al/03nov96/1340	569	5b	3.277	3822.8
w158c4r/I2	al/1487	w158c4r/butthead/al/05nov96/0938	70	0n	3.279	3752.4
w158c4r/I2	si/1740	w158c4r/butthead/si/05nov96/1241	572	7b	3.322	1693.6
w158c4r/I2	cl/2622	w158c4r/butthead/cl/03nov96/0844	668	6b	3.277	2408.4
w158c4r/I2	cl/2622	w158c4r/butthead/cl/03nov96/0950	299	1b	3.277	2416.4
w158c4r/I2	cl/2622	w158c4r/butthead/cl/05nov96/0955	99	0n	3.277	2370.4
w158c4r/I2	fe55/5894	w158c4r/butthead/fe55/27oct96/1921	788	4b	3.277	2820.8
w158c4r/I2	fe/6399	w158c4r/butthead/fe/03nov96/1416	646	4b	3.277	4259.2
w158c4r/I2	co/6925	w158c4r/butthead/co/03nov96/1250	99	1b	3.277	3800
w158c4r/I2	co/6925	w158c4r/butthead/co/03nov96/1301	646	4b	3.277	3813.6
w158c4r/I2	ni/7471	w158c4r/butthead/ni/03nov96/1032	591	6b	3.278	3229.6
w158c4r/I2	ni/7471	w158c4r/butthead/ni/03nov96/1108	136	4b	3.277	3229.2
w158c4r/I2	zn/8630	w158c4r/butthead/zn/03nov96/1527	516	4b	3.278	2474.8
w158c4r/I2	zn/8630	w158c4r/butthead/zn/03nov96/1558	647	3b	3.278	2469.6
w158c4r/I2	ge/9875	w158c4r/butthead/ge/03nov96/1121	659	6b	3.277	1952.4
w158c4r/I2	ge/9875	w158c4r/butthead/ge/03nov96/1158	651	NA	3.277	1963.2
w158c4r/I2	ge/9875	w158c4r/butthead/ge/03nov96/1234	184	1b	3.277	1966.8

Table 1.11: w158c4r/I2 CSR Spectral Resolution Data Sets

Chip	Target/Energy eV	Directory	Accepted Frames	Rejected Frames	Frame Time (seconds)	Counts per Frame
w215c2r/I3	al/1487	w215c2r/beavis/al/06jan97/2044	550	0n	3.277	4578.8
w215c2r/I3	cl/2622	w215c2r/beavis/cl/06jan97/2002	547	2b	3.277	2423.6
w215c2r/I3	ti/4509	w215c2r/beavis/ti/11jan97/1109	561	6b	3.329	5134.8
w215c2r/I3	v/4949	w215c2r/beavis/v/06jan97/2212	497	3b	3.277	4760.4
w215c2r/I3	v/4949	w215c2r/beavis/v/10jan97/2250	25	0n	3.277	4717.2
w215c2r/I3	fe/6399	w215c2r/beavis/fe/06jan97/2136	564	6b	3.277	4187.6
w215c2r/I3	fe/6399	w215c2r/beavis/fe/10jan97/2233	25	0n	3.277	4148.4
w215c2r/I3	co/6925	w215c2r/beavis/co/06jan97/0106	622	0n	3.277	3788.4
w215c2r/I3	co/6925	w215c2r/beavis/co/10jan97/2258	25	0n	3.277	3815.6
w215c2r/I3	ni/7471	w215c2r/beavis/ni/06jan97/0056	100	0n	3.277	3342
w215c2r/I3	ni/7471	w215c2r/beavis/ni/06jan97/2356	648	2b	3.277	3371.6
w215c2r/I3	zn/8630	w215c2r/beavis/zn/06jan97/2254	645	4b	3.277	2580.4
w215c2r/I3	zn/8630	w215c2r/beavis/zn/10jan97/2150	299	1b	3.277	2678.8
w215c2r/I3	ge/9875	w215c2r/beavis/ge/06jan97/1812	598	1b	3.277	1925.6
w215c2r/I3	ge/9875	w215c2r/beavis/ge/06jan97/1922	596	4b	3.277	1984
w215c2r/I3	ge/9875	w215c2r/beavis/ge/12jan97/1359	74	1b	3.277	1954

Table 1.12: w215c2r/I3 CSR Spectral Resolution Data Sets

Chip	Target/Energy eV	Directory	Accepted Frames	Rejected Frames	Frame Time (seconds)	Counts per Frame
w168c4r/S0	o/525	w168c4r/beavis/o/15dec96/1247	595	5b	7.149	3372
w168c4r/S0	al/1487	w168c4r/beavis/al/14dec96/1914	574	1b	3.277	4483.2
w168c4r/S0	al/1487	w168c4r/beavis/al/20dec96/2018	542	4b	3.277	4524
w168c4r/S0	cl/2622	w168c4r/beavis/cl/14dec96/2027	545	4b	3.277	2347.6
w168c4r/S0	cl/2622	w168c4r/beavis/cl/20dec96/2059	546	1b	3.277	2376.4
w168c4r/S0	v/4949	w168c4r/beavis/v/21dec96/1052	499	1b	3.277	4701.6
w168c4r/S0	v/4949	w168c4r/beavis/v/21dec96/1732	98	2b	3.277	4772.8
w168c4r/S0	fe/6399	w168c4r/beavis/fe/14dec96/2119	573	1b	3.274	4135.6
w168c4r/S0	co/6925	w168c4r/beavis/co/21dec96/1136	611	5b	3.278	3735.2
w168c4r/S0	co/6925	w168c4r/beavis/co/21dec96/1651	100	0n	3.277	3678.4
w168c4r/S0	ni/7471	w168c4r/beavis/ni/21dec96/1219	647	0n	3.277	3203.2
w168c4r/S0	ni/7471	w168c4r/beavis/ni/21dec96/1401	147	2b	3.277	3213.6
w168c4r/S0	zn/8630	w168c4r/beavis/zn/21dec96/1420	647	2b	3.277	2587.6
w168c4r/S0	zn/8630	w168c4r/beavis/zn/21dec96/1814	456	3b	3.277	2653.6
w168c4r/S0	ge/9875	w168c4r/beavis/ge/14dec96/2212	398	0n	3.277	1947.6
w168c4r/S0	ge/9875	w168c4r/beavis/ge/21dec96/0909	592	9b	3.277	1927.2
w168c4r/S0	ge/9875	w168c4r/beavis/ge/21dec96/0956	647	3b	3.277	1900.8

Table 1.13: w168c4r/S0 CSR Spectral Resolution Data Sets

Chip	Target/Energy	Directory eV	Accepted Frames	Rejected Frames	Frame Time (seconds)	Counts per Frame
w140c4r/S1	al/1487	w140c4r/butthead/al/20jan97/2041	647	2b	3.277	5247.6
w140c4r/S1	cl/2622	w140c4r/butthead/cl/20jan97/2131	647	1b	3.277	2819.2
w140c4r/S1	v/4949	w140c4r/butthead/v/24jan97/2106	650	0n	3.277	4092.8
w140c4r/S1	fe55/5894	w140c4r/butthead/fe55/24jan97/1901	645	3b	3.277	2444.8
w140c4r/S1	fe/6399	w140c4r/butthead/fe/23jan97/0752	649	1b	3.277	4294.4
w140c4r/S1	co/6925	w140c4r/butthead/co/24jan97/2157	649	1b	3.277	2689.6
w140c4r/S1	co/6925	w140c4r/butthead/co/28jan97/0916	321	4b	3.277	2720.8
w140c4r/S1	ni/7471	w140c4r/butthead/ni/28jan97/1003	646	4b	3.277	4086.4
w140c4r/S1	ni/7471	w140c4r/butthead/ni/28jan97/1051	649	1b	3.277	4068.8
w140c4r/S1	zn/8630	w140c4r/butthead/zn/28jan97/1147	640	8b	3.277	3149.6
w140c4r/S1	zn/8630	w140c4r/butthead/zn/28jan97/1234	648	2b	3.277	3197.2
w140c4r/S1	ge/9875	w140c4r/butthead/ge/23jan97/0837	646un	nun	0un	3004un
w140c4r/S1	ge/9875	w140c4r/butthead/ge/23jan97/0920	644un	nun	0un	3008.4un

Table 1.14: w140c4r/S1 CSR Spectral Resolution Data Sets

Chip	Target/Energy	Directory eV	Accepted Frames	Rejected Frames	Frame Time (seconds)	Counts per Frame
w182c4r/S2	al/1487	w182c4r/butthead/al/21dec96/1948	561	10b	3.277	4655.2
w182c4r/S2	cl/2622	w182c4r/butthead/cl/21dec96/2029	634	6b	3.277	2390.8
w182c4r/S2	cl/2622	w182c4r/butthead/cl/21dec96/2115	315	4b	3.277	2392.4
w182c4r/S2	v/4949	w182c4r/butthead/v/02jan97/1321	521	4b	3.277	5554
w182c4r/S2	fe/6399	w182c4r/butthead/fe/21dec96/2146	627	5n	3.277	4386.4
w182c4r/S2	co/6925	w182c4r/butthead/co/02jan97/1503	644	4b	3.277	3538
w182c4r/S2	co/6925	w182c4r/butthead/co/02jan97/1802	149	1b	3.277	4058.4
w182c4r/S2	ni/7471	w182c4r/butthead/ni/02jan97/1548	642	8b	3.277	3430.8
w182c4r/S2	ni/7471	w182c4r/butthead/ni/02jan97/1755	148	2b	3.277	3455.2
w182c4r/S2	zn/8630	w182c4r/butthead/zn/02jan97/1631	645	3b	3.277	2708
w182c4r/S2	zn/8630	w182c4r/butthead/zn/02jan97/1718	519	3b	3.277	2707.2
w182c4r/S2	ge/9875	w182c4r/butthead/ge/02jan97/1234	639	9b	3.277	2118.8
w182c4r/S2	ge/9875	w182c4r/butthead/ge/02jan97/1359	645	5b	3.277	2096

Table 1.15: w182c4r/S2 CSR Spectral Resolution Data Sets

Chip	Target/Energy	Directory eV	Accepted Frames	Rejected Frames	Frame Time (seconds)	Counts per Frame
w134c4r/S3	f/677	w134c4r/butthead/f/03feb97/1151	587	0n	7.148	5260
w134c4r/S3	al/1487	w134c4r/butthead/al/01feb97/1941	646	2b	3.277	5342.4
w134c4r/S3	cl/2622	w134c4r/butthead/cl/01feb97/2024	649	1b	3.277	2907.6
w134c4r/S3	v/4949	w134c4r/butthead/v/05feb97/1840	646	4b	3.277	4664
w134c4r/S3	fe/6399	w134c4r/butthead/fe/01feb97/2110	648	2b	3.277	3615.6
w134c4r/S3	fe/6399	w134c4r/butthead/fe/05feb97/1811	100	0n	3.277	3603.6
w134c4r/S3	co/6925	w134c4r/butthead/co/05feb97/1923	641	2b	3.277	4505.6
w134c4r/S3	ni/7471	w134c4r/butthead/ni/05feb97/1457	644	2b	3.277	4457.2
w134c4r/S3	zn/8630	w134c4r/butthead/zn/05feb97/1547	647	1b	3.277	3623.2
w134c4r/S3	zn/8630	w134c4r/butthead/zn/05feb97/1825	99	0n	3.277	3618.8
w134c4r/S3	ge/9875	w134c4r/butthead/ge/01feb97/2152	647	3b	3.277	1733.2
w134c4r/S3	ge/9875	w134c4r/butthead/ge/05feb97/1638	649	1b	3.277	3394.8
w134c4r/S3	ge/9875	w134c4r/butthead/ge/05feb97/1749	100	0n	3.277	3453.6

Table 1.16: w134c4r/S3 CSR Spectral Resolution Data Sets

Chip	Target/Energy	Directory eV	Accepted Frames	Rejected Frames	Frame Time (seconds)	Counts per Frame
w457c4/S4	al/1487	w457c4/beavis/al/02dec96/1024	544	6b	3.277	4634.8
w457c4/S4	cl/2622	w457c4/beavis/cl/02dec96/1155	547	3b	3.277	2405.2
w457c4/S4	v/4949	w457c4/beavis/v/02dec96/0128	49	0n	3.277	4830.8
w457c4/S4	v/4949	w457c4/beavis/v/02dec96/0135	48	1b	3.285	4878.4
w457c4/S4	v/4949	w457c4/beavis/v/02dec96/1424	498	1b	3.277	4807.2
w457c4/S4	fe/6399	w457c4/beavis/fe/02dec96/1236	566	4b	3.277	4151.6
w457c4/S4	co/6925	w457c4/beavis/co/02dec96/1500	624	6b	3.277	3995.6
w457c4/S4	ni/7471	w457c4/beavis/ni/02dec96/1638	639	5b	3.278	3516.8
w457c4/S4	ni/7471	w457c4/beavis/ni/02dec96/1832	98	2b	3.277	3544.4
w457c4/S4	zn/8630	w457c4/beavis/zn/02dec96/1726	644	4b	3.277	2906
w457c4/S4	zn/8630	w457c4/beavis/zn/02dec96/1813	249	1b	3.277	2916
w457c4/S4	ge/9875	w457c4/beavis/ge/02dec96/1318	596	1n	3.277	2144.8
w457c4/S4	ge/9875	w457c4/beavis/ge/02dec96/1547	596	4b	3.277	2234.8

Table 1.17: w457c4/S4 CSR Spectral Resolution Data Sets

Chip	Target/Energy	Directory eV	Accepted Frames	Rejected Frames	Frame Time (seconds)	Counts per Frame
w201c3r/S5	al/1487	w201c3r/beavis/al/13dec96/0945	648	2b	3.277	4487.2
w201c3r/S5	cl/2622	w201c3r/beavis/cl/13dec96/1026	642	5b	3.278	2405.6
w201c3r/S5	v/4949	w201c3r/beavis/v/13dec96/1400	636	2b	3.277	4812.4
w201c3r/S5	fe/6399	w201c3r/beavis/fe/13dec96/1106	627	4b	3.278	4324
w201c3r/S5	co/6925	w201c3r/beavis/co/13dec96/1463	647	3b	3.277	3965.2
w201c3r/S5	ni/7471	w201c3r/beavis/ni/13dec96/1531	649	1b	3.277	3521.2
w201c3r/S5	ni/7471	w201c3r/beavis/ni/13dec96/1613	298	2b	3.277	3526
w201c3r/S5	zn/8630	w201c3r/beavis/zn/13dec96/1655	649	1b	3.277	2868.8
w201c3r/S5	zn/8630	w201c3r/beavis/zn/13dec96/1735	300	0n	3.277	2873.6
w201c3r/S5	ge/9875	w201c3r/beavis/ge/13dec96/1147	645	5b	3.277	2192
w201c3r/S5	ge/9875	w201c3r/beavis/ge/13dec96/1229	649	0n	3.277	2177.2

Table 1.18: w201c3r/S5 CSR Spectral Resolution Data Sets

Data File	Description
*_rt.evlist	ACIS RV format eventlist
*_rt_bias_avg.fits	mean bias frame
*_bias.000?.fits	sample bias frames
*_frame.000?.fits	sample data frames
*.mca.summary	ascii file summarizing the dataset
*.mca.data	IDL save file including average overclock level, average overclock noise, total number of events, peak location, peak width, and number of events under the peak as a function of frame number.
*.mca.spec	IDL save file including number of events as a function of energy, quadrant, and grade, and an image of the g02346 events under the peak in 32x32 pixel bins.
products/*g0234_img.fits	number density map of detected events in g0234.
products/*g0.qdp	for each quadrant, the pulse height histogram of g0 events.
products/*g0234.qdp	for each quadrant, the pulse height histogram of g0234 events.
products/*g0234_lightcv.qdp	for each quadrant, g0234 count rate as a function of frame number.
prodcuts/*pcf.qdp	for each quadrant, pulse height histograms of each grade.
products/*neighborhist*.qdp	for each quadrant, histograms of corner, top, bottom, left, and right pixel distributions of detected events.

Table 1.19: CSR Database Products

1.3.2 Physics of low energy tail in the CCD response function

A response of the frontside illuminated CCDs to monochromatic X-rays shows a noticeable low energy tail in addition to the well understood main peak and escape and fluorescence features. It is generally assumed for silicon detectors that the tail's origin is due to dead layer on the surface of the device [21, 23]. We have studied the response of the CCD to the monochromatic synchrotron X-rays at BESSY in a wide range of energies and have discovered an unknown feature in the very low energy part of the response function (see [29, 28]). Examining changes in its behavior as a function of energy of incoming radiation we came to the conclusion that it originates from the photons interacting in the gate insulator, which is not a dead layer as was previously thought. We have developed a model that explains the shape of this newly discovered feature as well as the shape of entire low energy tail in the CCD response function.

1.3.2.1 Experimental

Experimental data were acquired at the electron storage ring BESSY (Berlin), where device cooled down to -120^o C was illuminated with monochromatized synchrotron X-rays. The data were taken at the KMC (Krystal MonoChromator) beamline in a wide range of energies from 1487 eV to 5898 eV with the emphasis on the understanding of the device behavior around silicon absorption K edge (1836 eV). That explains the choice of the energy data points for this measurement having higher density around silicon K edge: 1487, 1700, 1740, 1800, 1825, 1832, 1835, 1836.5, 1838, 1840, 1842, 1845, 1847, 1855, 1870, 1900, 2015, 2309, 2622, 3313, 3691, 4090, 4510, 4952, 5414, and 5898 eV. A typical exposure time at each energy was 4000 seconds, with 5 times that amount for the 2015 eV measurement.

Device was clocked by the ACIS electronics with serial register clock frequency of 100 kHz, total system noise at this frequency being about 2 electrons rms. Very low system noise was the crucial factor that allowed us to observe the low energy features discussed below.

1.3.2.2 Escape and fluorescence peaks

At X-ray energies greater than silicon K absorption edge, which we have measured for crystalline silicon to be 1839 eV, the response function of the device shows two distinct peaks in addition to the primary one. One of them at energy $E_f = 1739$ eV is due to the silicon fluorescent photons that have escaped far enough from the original site of interaction to be detected as a separate event. The other peak centered at energy $E_e = E_0 - E_f$, where E_0 is energy of the incident photon, is called an escape peak. It is formed by the electron clouds that are left when the flourescent photon carrying away energy E_f leaves silicon substrate or, again, is stopped far enough to be detected separately. The behavior of these peaks is reasonably well described by the model developed as a part of ACIS calibration program and is discussed in more detail in section 1.14. The relative amplitudes of these peaks as a function of energy, both experimentally measured and simulated, are shown in Fig. 1.128.

1.3.2.3 Low energy peak

On Fig. 1.8 is shown the histogram of the CCD response to the monochromatic flux of 1700

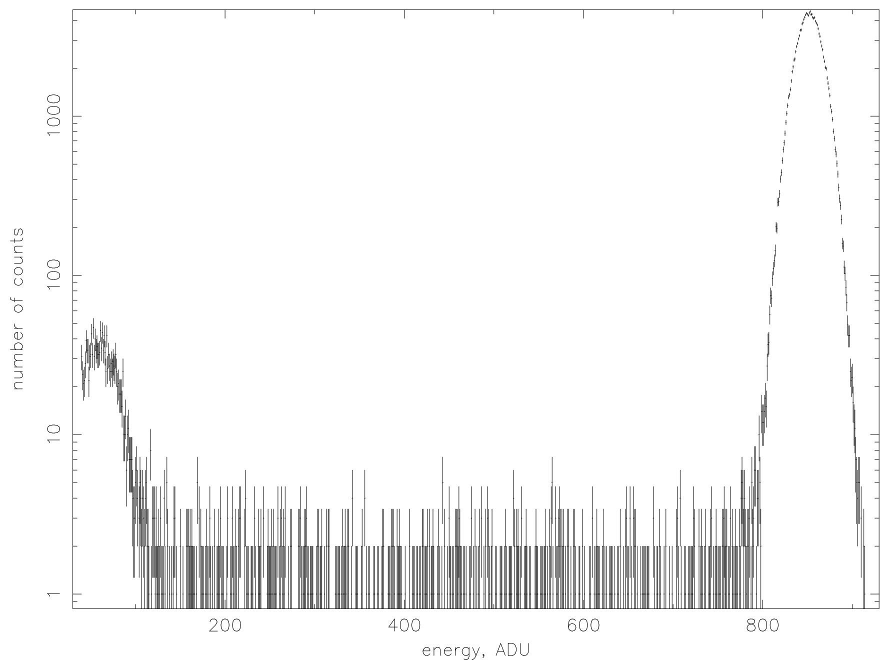

Figure 1.8: Histogram of the CCD response to 1700 eV X-rays.

eV X-rays, this histogram is typical for the device response at energies below the silicon absorption K edge (1841 eV). It has two distinct peaks - the main one which corresponds to the energy of the incoming photons, and the second one at energy which constitutes 7% of the main peak energy. Notice that since 1700 eV is below the silicon K absorption edge energy, silicon fluorescence does not play any role here.

The shape of the low energy peak is not quite gaussian, though it is possible to make a gaussian fit of reasonable quality. Having done that at different energies we found that the centroid of the low energy peak moves approximately proportionally to the centroid of the main peak (which is known to be a linear function of the energy of irradiating photons), as it is shown in Fig 1.9. Such behavior is different, for instance, from the silicon escape

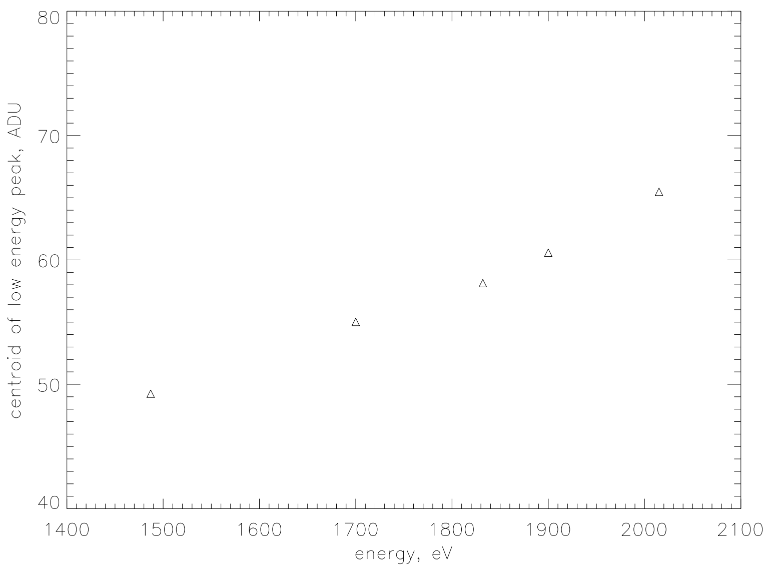

Figure 1.9: Centroid of the low energy peak as a function of energy.

peak for which energy shift is exactly the same as for the main peak.

Another important observation is that total number of counts in the low energy peak is consistent with the number of calculated photon interactions within the gate isolator.

If we assume that the gate insulator consists of a layer of SiO_2 with thickness d_{ox} and characteristic absorption length λ_{ox}, the number of photons per unit area N_{ox} absorbed in it is

$$N_{ox} = N_0(1 - \exp{(-\frac{d_{ox}}{\lambda_{ox}})}) \tag{1.6}$$

where N_0 is photon flux enetering SiO_2 layer. The number of photons N_{si} that are absorbed inside the volume of silicon and form the main peak in the histogram equals simply entire flux of photons entering silicon in the case when thickness of the depleted layer of silicon d_d is big compared to the characteristic absorption length in silicon λ_{si}. Due to attenuation in the gate oxide $N_{si} = N_0 \exp{(-\frac{d_{ox}}{\lambda_{ox}})}$. This gives the ratio of the intensities for the two peaks:

$$\frac{N_{ox}}{N_{si}} = (e^{\frac{d_{ox}}{\lambda_{ox}}} - 1) \tag{1.7}$$

In the case $d_{ox} \ll \lambda_{ox}$ which is definitely true at energies below silicon absorption K edge, formula (1.7) comes to

$$\frac{N_{ox}}{N_{si}} = \frac{d_{ox}}{\lambda_{ox}} \tag{1.8}$$

In Fig. 1.10 is shown the ratio of the number of events in the low energy peak to the number of events in the main peak as a function of energy. The dashed line in this Figure

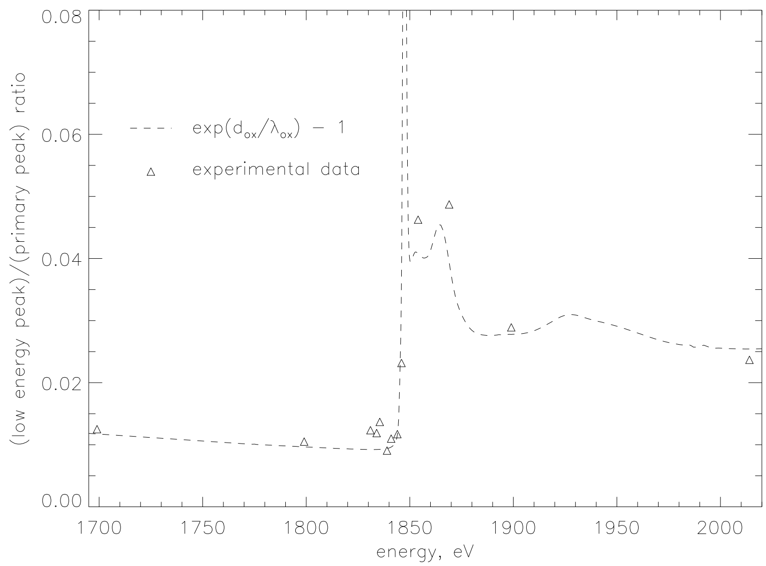

Figure 1.10: Ratio of number of counts in low energy peak and in the primary peak as a function of energy, calculated (dashed line), and measured (triangles).

is the result of the calculation according to equation 1.7. The dependence of λ_{ox} on energy comes from our high precision experimental measurement (see [25]) and includes all the details of the near edge absorption structure. The relative number of counts in the low energy peak jumps up sharply at the energy corresponding to the silicon K absorption edge, in full agreement with the prediction of the formula 1.7.

The most remarkable feature of this plot is that the jump occurs at the energy corresponding to the silicon absorption edge in SiO_2, which is different from the silicon absorption edge in the crystalline silicon. We have shown in [25] that there exists a 6 eV shift between the silicon absorption edge energies in Si and SiO_2. Three data points on Fig 1.10 in between the two edges staying at the same level as the points below the edge in Si prove most reliably that the low energy peak originates in the SiO_2 layer.

Unlike diode-type detectors such as Si(Li) [21] or $p$$-$$n$ junction CCD [23], buried channel CCDs have an electric field in the gate oxide covering silicon surface. In Fig. 1.11 is shown a distribution of the potential in the gate structure of the buried channel CCD. It is clear from this figure that electrons generated in the SiO_2 layer adjacent to the silicon substrate will be travelling towards the collecting potential well of the CCD. Charge created in the Si_3N_4 and other layers sitting on the top of it will be lost. The mobility of the electrons in silicon dioxide, although lower than in silicon by roughly an order of magnitude, is still high enough to allow the photogenerated charge to get collected in a frame time.

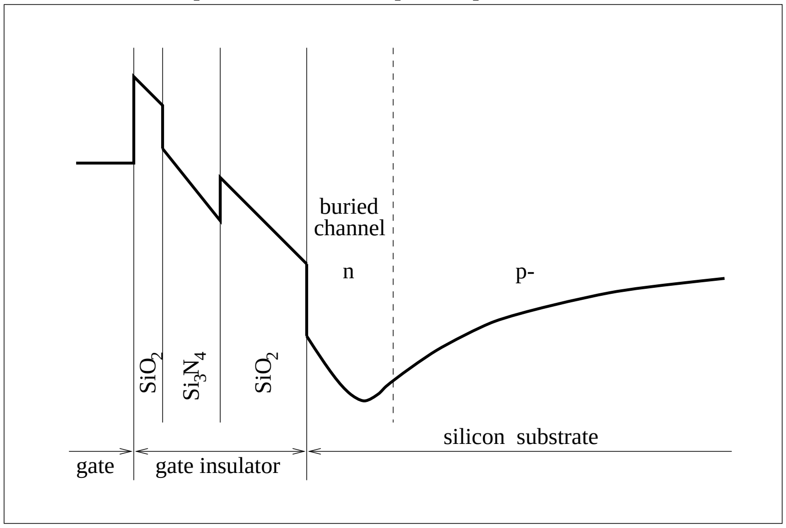

Figure 1.11: Potential distribution in the buried channel CCD.

All these facts lead to the unambiguous conclusion that the low energy peak's origin is due to the photons absorbed inside the gate insulator.

When an X-ray photon interacts with a material of the gate oxide layer, it generates a cloud of electron-hole pairs. Since the bandgap of SiO_2 is approximately 9 eV (as opposed to 1.12 eV in silicon), the amount of electrons created by one photon is approximately an order of magnitude lower than for silicon-absorbed photons. As a result the corresponding peak in a histogram is seen at very low energy.

So far we have discussed only data taken at energies around silicon K edge. The picture is very different at higher energies. At 5414 eV (a histogram of the device response is shown on Fig. 1.12) instead of the well-defined low energy peak shifted further up from what we see at 1700 eV histogram, there is a broad elevation which goes all the way down to the noise peak (not shown) without reaching a maximum. We believe that the reason for such behavior is an increased electron cloud size at higher energies. It is known that the diameter of an electron cloud generated by a photon increases with energy and according to various authors could be tens or even hundreds of nanometers at several keV [21, 23, 26]. The gate oxide layer is very thin, approximately 70 nm and its thickness is comparable to the cloud size. When the cloud diameter exceeds the oxide thickness, for any cloud originated in silicon dioxide part of the charge will end up either in silicon, or in silicon nitride and the amount of that charge depends on the photon's depth of interaction. There exists a potential barrier for the electrons that are moving from Si_3N_4 into SiO_2 (see Fig. 1.11), which means that part of the cloud that enters Si_3N_4 will be almost entirely lost.

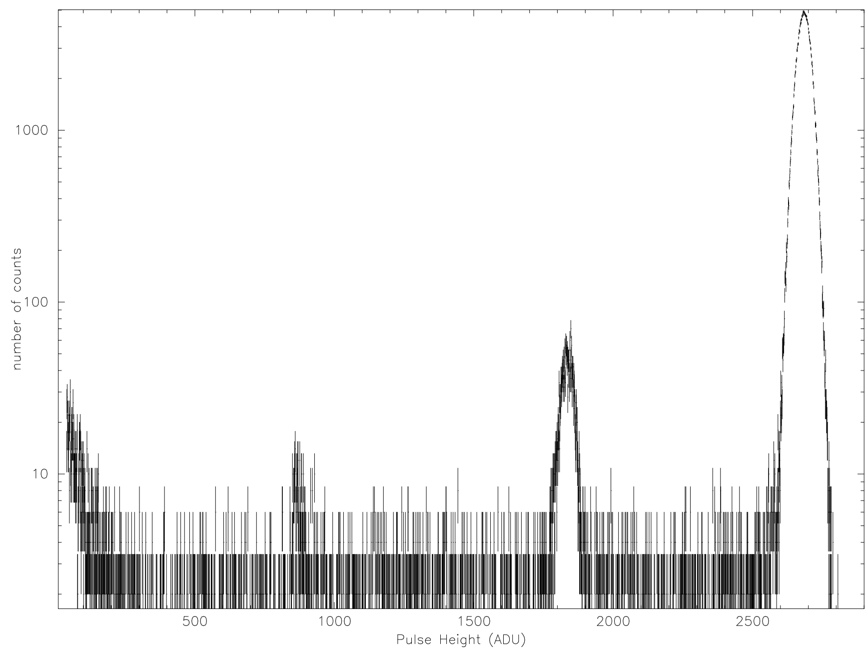

Figure 1.12: Histogram of the CCD response to 5414 eV X-rays.

For the events that originate in Si_3N_4 only electrons with sufficiently high enough energy can overcome the potential barrier.

Thus, even small changes in the depth of interaction of the original photon in the SiO_2 layer lead to significant changes in the total number of electrons collected, and as a result the low energy peak is washed out into a much broader feature without an extremum.

1.3.2.4 Shape of the entire low energy tail

A similar phenomenon - splitting of the electron cloud between silicon and silicon dioxide - should obviously take place for any cloud which originates within the distance R from the $Si - SiO_2$ interface, where R is the cloud radius. Since the number of the electron-hole pairs generated per eV of the incoming photon energy is significantly higher in silicon than in silicon dioxide, the amplitude of such events will change gradually from the primary peak down to the low energy peak, as the center of the cloud moves from silicon into oxide. This is schematically shown in Fig. 1.13, which explains how the low energy tail of the spectral redistribution function is formed. Fig. 1.14 provides evidence that the entire low energy tail comes from the photons interacting within a small distance from the silicon interface. This figure shows the fraction of the events in the tail as a function of the characteristic absorption length λ_{si} in silicon. In order to produce this plot events in the fluorescent and

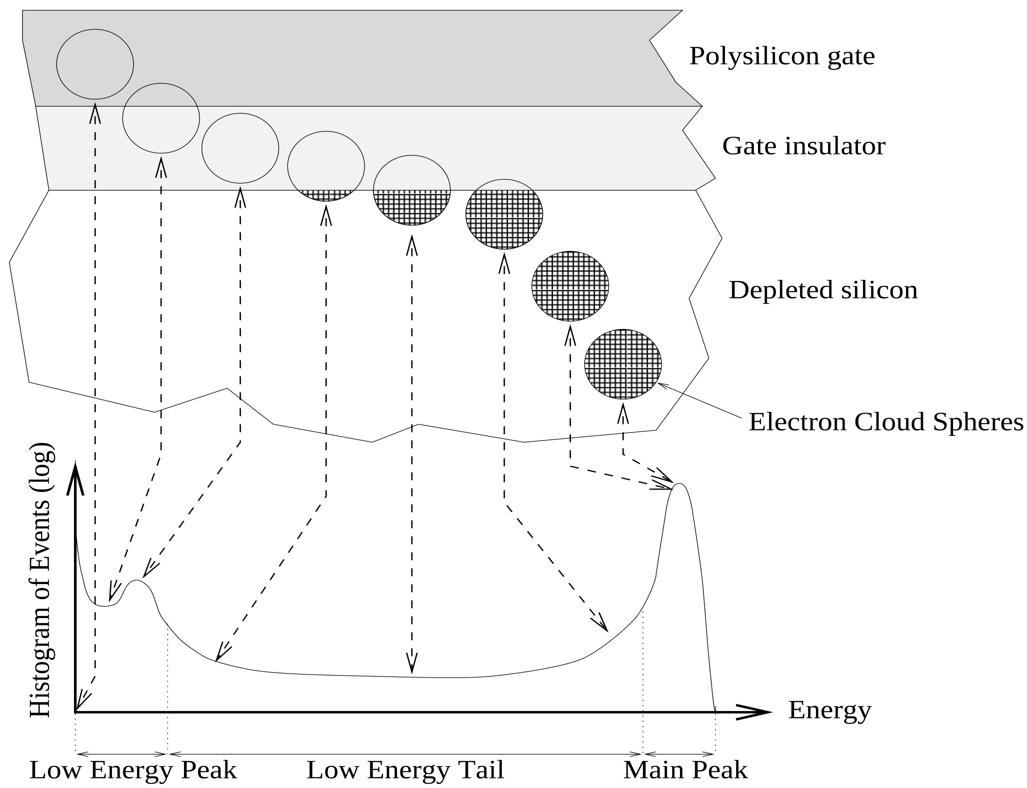

Figure 1.13: Scheme of forming low energy tail from the electron clouds generated close to $Si - SiO_2$ interface.

in the escape peaks were ignored, as well as the low energy (oxide) peak events discussed above. Each point in this plot corresponds to a measurement at a particular energy, and the points are connected sequentially in energy ascending order, starting at the lowest energy point labeled 1487 eV. The plot demonstrates that for widely separated energies (for instance, 1487, 1836, and 3600 eV) with the similar valaues of λ_{si} the fraction of events in the tail is similar. Moreover, immediately above the silicon edge, at very small λ_{si}, the tail intensity goes up sharply. If one makes a very crude assumption that the cloud radius R is constant (or slowly changing function of energy in the range of interest), then an approximately $1/\lambda_{si}$ dependence is an indication that the flat part of the tail results from the the photons interacting in a shallow region near the surface, whose thickness $2R$ is small compared to λ_{si}.

If all the events in the flat part of the low energy tail come from the electron clouds formed within a distance R from the $Si - SiO_2$ interface, the fraction of the events in the flat part of the tail can be used to determine the electron cloud size. The results of such

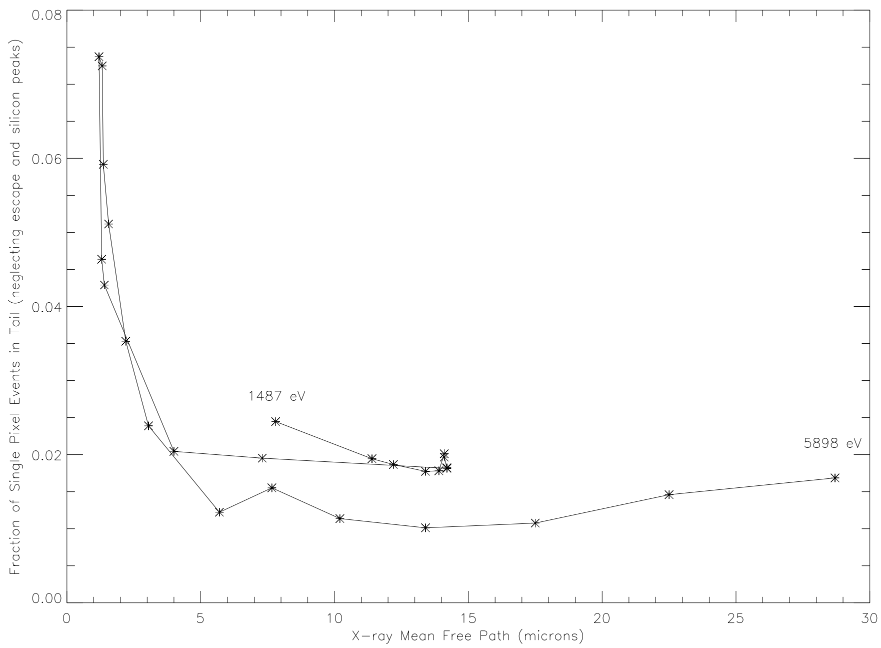

Figure 1.14: Fraction of single pixel events in tail as a function of characteristic absorption length in silicon.

calculations are shown on Fig. 1.15. The values of cloud sizes are significantly lower than 150 – 200 nm reported in [21, 23]. They also are much smaller than cloud sizes in the bulk silicon extracted from our mesh experiments [27]. We believe the reason for this large discrepancy is the presence of a potential barrier for electrons at the $Si - SiO_2$ interface.

Electron cloud generation starts with emission of relatively high energy primary photo- and Auger electrons which dissipate their energy in an ionization cascade. The range of electrons in the initial stages of the cascade is roughly consistent with the cloud radius in our model. It is the low energy, nearly thermalized electrons with sharply increased mean free path (of an order of 100 nm), that are responsible for the large cloud sizes quoted in [21, 23]. In the MOS structure analyzed here a "potential wall" at the $Si - SiO_2$ interface prevents the low energy electrons from penetrating into the SiO_2 for the clouds centered at a distance greater than R from this interface. Only hot electrons in the initial stages of cascading (for which the range is very small) can participate in the cloud splitting between the silicon and the silicon dioxide. This feature of the buried channel MOS X-ray CCDs is very beneficial for the spectrometric properties of the frontside illuminated CCDs, since it results in larger fraction of counts going into the main peak instead of the tail, and, hence, better energy resolution and quantum efficiency.

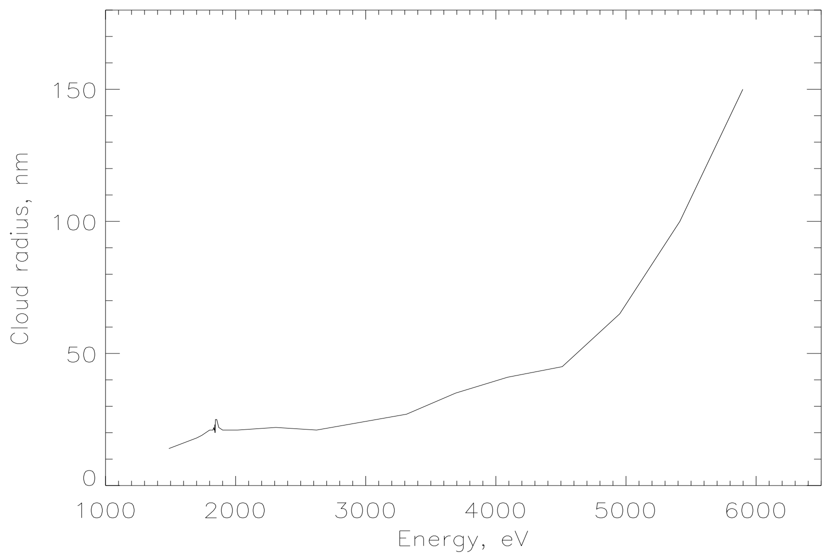

Figure 1.15: Cloud radius in silicon as a function of energy.

The precise shape of the tail depends on the density distribution of charge in the cloud and this distribution in principle can be extracted. We have not accomplished this task yet, because it requires much higher number of counts than we were able to obtain during the limited time at the synchrotron facility.

We have developed a model based on the scheme shown at Fig. 1.13. The basic assumption is that each electron cloud is a sphere and when the sphere crosses the silicon interface, the number of electrons produced in each material is proportional to the volume of the corresponding segment of the sphere. Each material is assumed to have different electron-hole creation energy. This is equivalent to assuming that electrons have the same mean free path in both materials. This may be not such a bad approximation, especially for high energy electrons in the original stages of cascading. As discussed above, electrons liberated in the oxide contribute to the total charge collected. From the low energy peak position (see Fig. 1.9) we deduce an effective electron-hole pair creation energy w_{ox} in SiO_2 of approximately 52 eV. This value includes recombination losses and hence differs significantly from the reported value of 17 eV/pair. We have made no attempt here to decouple the true value of w_{ox} and the losses. This matter is clearly worth pursuing, because it will allow to produce a more accurate model of the device response.

In Fig. 1.16 - 1.19 are shown the results of the best fit of the model to the data at several energies.

The results of the this section are used as the basis for the model of the CCD described

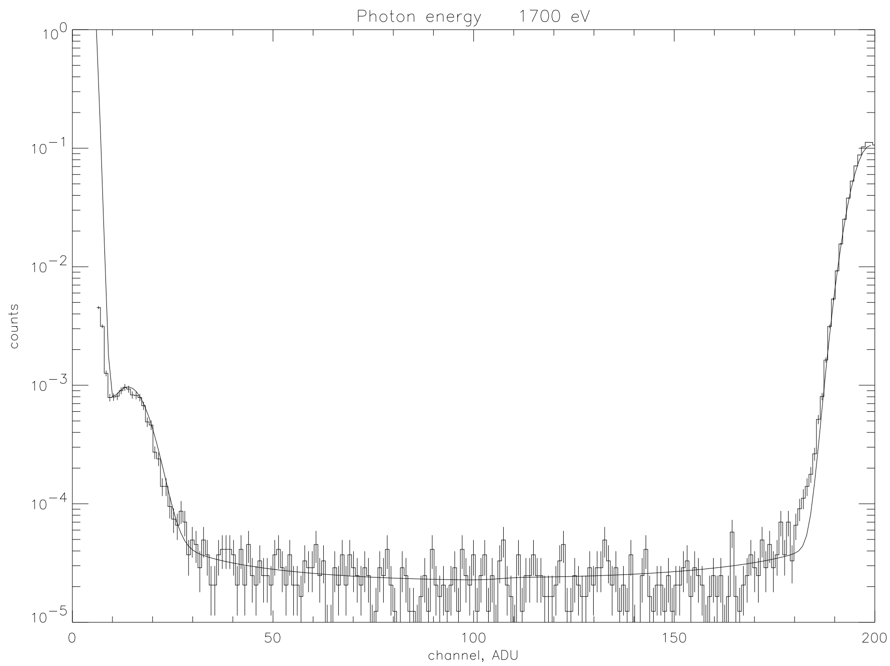

Figure 1.16: Response of the CCD to the 1700 eV photons and the model prediction.

in section 1.14 to produce a response matrix of the flight devices.

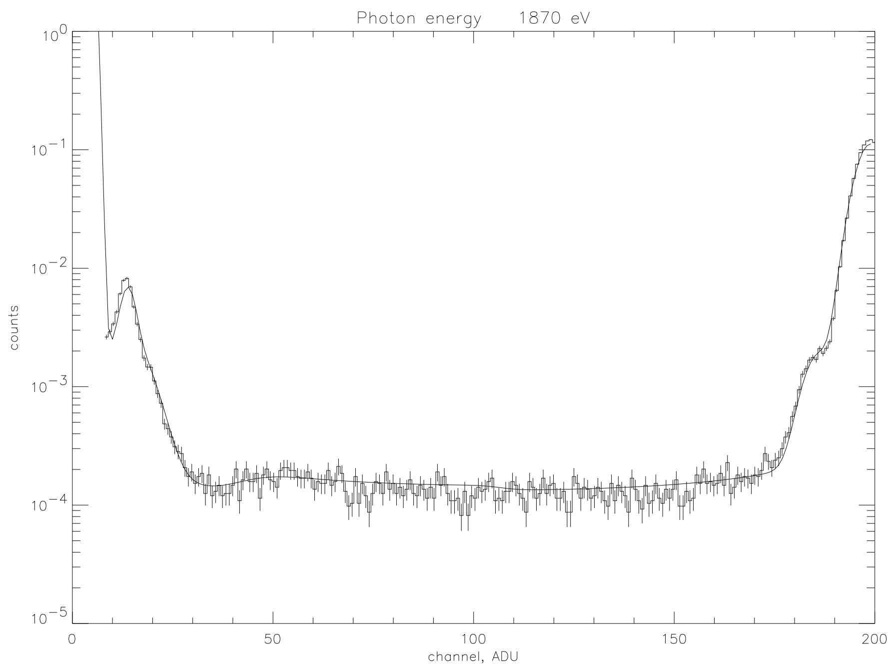

Figure 1.17: Response of the CCD to the 1870 eV photons and the model prediction.

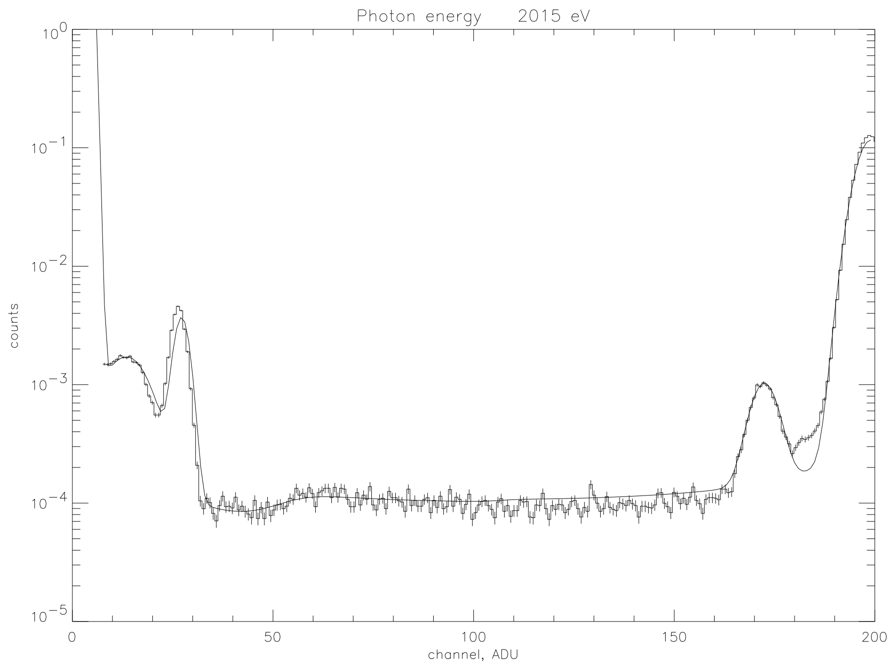

Figure 1.18: Response of the CCD to the 2015 eV photons and the model prediction.

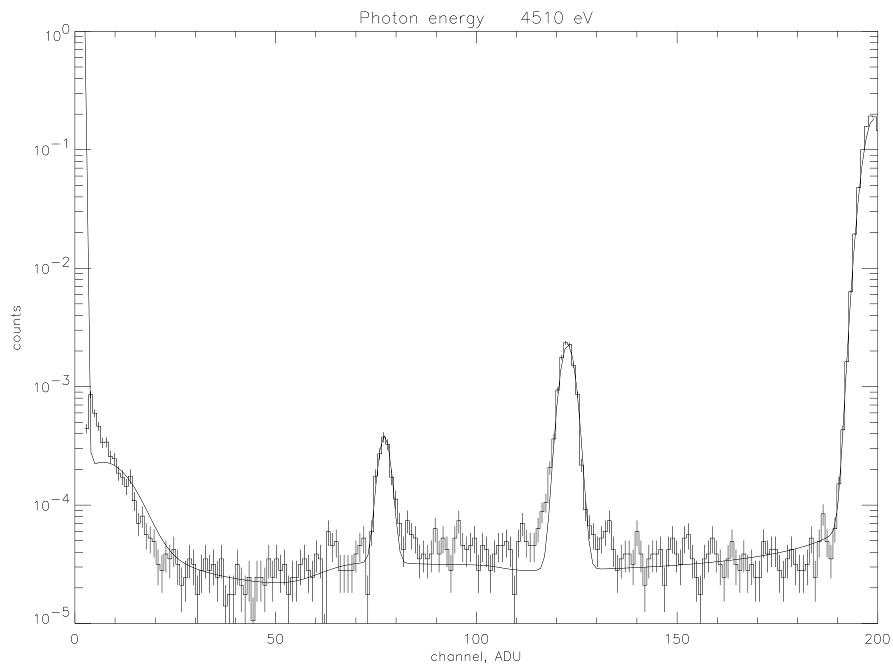

Figure 1.19: Response of the CCD to the 4510 eV photons and the model prediction.